Interphase energies of hcp precipitates in fcc metals: A density-functional theory study in Al-Ag

Daniel Finkenstadt[1,2,*] and D. D. Johnson[3,†]
[1]*Physics Department, U.S. Naval Academy, Annapolis, Maryland 21402, USA*
[2]*U.S. Naval Research Laboratory, Code 6390, Washington, DC 20375, USA*
[3]*Department of Materials Science & Engineering and Department of Physics, University of Illinois at Urbana–Champaign, Urbana, Illinois 61801, USA*

(Received 16 October 2009; revised manuscript received 2 January 2010; published 28 January 2010)

Density-functional theory (DFT) calculations of interphase boundary energies relevant to hexagonal-close-packed (hcp) γ-precipitate formation were performed within approximate unit cells that mirror the experimental conditions in face-centered-cubic (fcc) Al-Ag solid solutions. In Al-rich, fcc Al-Ag, γ precipitates are observed to form rapidly with large (300+) aspect ratios even though the Al stacking-fault energy is high (approximately 130 mJ/m^2), which should suppress hcp ribbon formation according to standard arguments. Our DFT results show why high-aspect ratio plates occur and why previous estimates based on Wulff construction were orders of magnitude less than observed values. Using DFT, we obtain a Gibbs free-energy diagram that gives the relevant hcp equilibrium precipitate structure occurring at 50 at. % Ag. We derive the critical nucleation parameters for γ-precipitate formation, which require our calculated bulk-driving force for nucleation and interphase boundary energies. From our DFT-based *non*equilibrium estimate for precipitation that accounts for growth via coarsening by ledge and edge migrations, we obtain time-dependent aspect ratio that agrees well with experiment. The same energetics and growth model are relevant to other phenomena, such as lath morphology in martensites or island coarsening.

DOI: 10.1103/PhysRevB.81.014113 PACS number(s): 81.30.Mh, 61.72.Nn, 64.70.kd

I. INTRODUCTION

Aluminum-silver (Al-Ag) alloys are a prototype for precipitation, nucleation and growth, and surface-island phenomena. In 1938, Gunier[1] and Preston[2] discovered the so-called GP zones in Al-rich, fcc Al-Cu (platelike precipitates) and later Al-Ag (spherical precipitates).[3] This led to the eventual discovery[4] of γ-plate precipitates in Al-Ag [a solute-rich hexagonal-close-packed (hcp) phase inside of face-centered-cubic (fcc) solid solution] that lengthen rapidly upon annealing (up to micron sizes within hundreds of seconds),[5] depending upon solute composition. Indeed, γ-plate precipitates are a textbook example of diffusional solid-solid transformation.[6] Moreover, the broad view of plate shapes,[7] which is not discussed as often as aspect ratio, shows that their triangular facets are similar to the triangular and oblong Ag islands that can be grown on Al (111) and on other surfaces,[8–11] a connection we discuss at the end.

Many models have been applied to the growth rates and shape-coarsening kinetics of platelike precipitates.[12–17] These efforts were often unsuccessful due, in part, to a lack of data on interphase energies, plate composition, and the nucleation driving force. Importantly, during precipitation interphase boundaries are formed, where two distinct phases are adjacent to each other, both of which can have dramatically different compositions and surface orientations. Generally, these solute effects and solubility limits can alter drastically the precipitation thermodynamics and the resulting mechanical strength versus composition, e.g., in Al-based alloys and Fe-Cu.[18] For precipitation, in the absence of direct data, some researchers extrapolated from pure Al to what the interphase energies would be in a dilute alloy. However, the stacking-fault energy (SFE) of pure Al is high (approxiamtely 130 mJ/m^2),[19–22] but the SFE is highly sensitive to solute,[20] due to the well-known Suzuki effect,[23–25] where, if a solute is energetically favored to reside at a SF, the SFE is lowered (sometimes dramatically) and defect formation is more favorable. More generally, any planar fault energy will reflect such energy-reducing interactions of solute and planar defects, as observed, e.g., for onset twinning stress in alloys.[25]

From the composition dependence of the interphase boundary energies, we have shown that a *local* versus *global* concentration of solute determines the reduction in SFE.[20] Also, the interphase energy for a given solute content in each phase determines the time dependence of the aspect ratio of γ plates, which has been measured in Al-Ag.[5] In addition, we have proposed an analytic model for precipitation and growth of solute-rich phases in dilute solid solutions (s.s.), where a low-strain shear transformation connects the two close-packed phases.[26] Given interphase energies (either from experiment or theory) and critical nucleation parameters, the model predicts the nonequilibrium shape and growth rates.

Therefore, given the limited availability, we present density-functional theory (DFT) results for formation enthalpies and interphase energies required to predict nonequilibrium γ-precipitate time-dependent growth for direct comparison to experiment. In Sec. II, we summarize the understanding of γ-plate precipitate growth and shape, building on previous models of growth[15] and shape development,[26] to establish the required quantities that can be extracted from DFT results. In Sec. III, we present how to calculate from DFT relevant formation enthalpies, defect energies, and interphase energies. In particular, we provide the ordered unit-cell approximates for direct comparison to experimentally observed traces of the γ plates[5] (see Fig. 1), which shows clearly the interface boundary at the precipitate and local solute depletion effects, as well as the aspect ratio. In Sec.

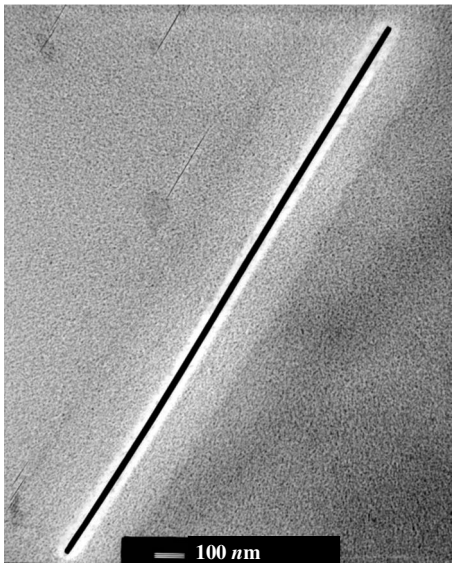

FIG. 1. TEM of high-aspect ratio hcp precipitate oriented along fcc ⟨111⟩ from Ref. 5. Dark regions have enhanced Ag concentration, with plate having 40–50 at. % Ag. Surrounding the hcp precipitate is fcc 4.2 at. % Ag solid solution with GP zones, except near plate, where Ag is depleted (Ref. 27).

IV, we discuss our DFT results for interphase energies, where energetics of γ nuclei are found to depend strongly on the small (0001)‖(111) interphase energy across hcp precipitates (0001) faces adjacent to the fcc (111) host planes. Our γ_{111} of 15 mJ/m^2 is substantially lower than the erroneous estimates using the 130 mJ/m^2 Al SFE at plate faces.[28] While this γ_{111} gives an equilibrium aspect ratio A_{eq} of ~20, that is, seven times larger than previous work, it is still tens times smaller than experiment. Thus, to address the nonequilibrium growth rate, we use free-energy arguments to obtain, in Sec. V, an estimate of the equilibrium precipitate composition X_γ of 0.50 at. % Ag, and ΔG_V [the entropic driving force Gibb's free-energy change per unit volume] and, in Sec. VI, the nucleation barrier ΔG^* of 1–4 eV. Before concluding in Sec. VIII, we provide an example of the generality of our model in Sec. VII by qualitatively describing how it would be applied to island growth on surfaces.

II. ENERGETICS AND THERMODYNAMICS OF ASPECT RATIO

The textbook prototype for platelike precipitates continues to be Al-Ag,[6] partly because it was observed early on in the development of microscopy techniques and partly because it has many simplifying characteristics that facilitate an analytic model. Among these simplifying features are the similar fcc lattice spacings of Al (4.05 Å) and Ag (4.09 Å), which preclude elastic strain effects,[29] while the dissimilar atomic numbers of Al and Ag make possible high-contrast transmission electron microscopy (TEM). Moreover, pure Al and Al-rich Al-Ag both exhibit a simple plane-strain transformation, connecting the α-fcc and γ-hcp. Recent microscopy experiments at 4 at. % Ag and 400 °C find plates of around 50 at. % Ag oriented along ⟨111⟩ directions in an

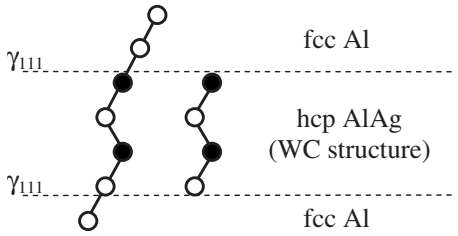

FIG. 2. Model of (111) precipitate interface projected onto (110) based on stacking-fault structure [isf-(ii) from Ref. 20] compared to (WC-like) alternating hcp. Open (filled) circles are Al (Ag).

Al-rich fcc matrix[5] (see dark rectangle in Fig. 1). Precipitates grow in seconds to minutes as the alloy is quenched from s.s., faster with increasing Ag content. Upon subsequent aging at 160 °C, spherical GP zones are grown throughout the fcc matrix away from the precipitate, making a clearly visible Ag-depleted zone (the light region surrounding the precipitate in Fig. 1). Observed plate compositions of 46 ± 4 at. % Ag are lower than supposed from the assessed equilibrium Al-Ag phase diagram[30] (i.e., 59 at. % Ag), and the observed plate aspect ratios (300+) are two orders of magnitude larger than expected from equilibrium estimates.[31–33] The actual structure of precipitates remains unknown. These microscopy experiments have allowed real-time determination of the plate aspect ratios, from which a simple analytic model can determine (indirectly) the ratio of the edge γ_{211} and face γ_{111} interface energies. However, the time variation in this ratio must also be examined in more detail, as these energies are static and are not able to explain the dynamic observed shapes[7] from first principles.

A. Equilibrium aspect ratio

Interestingly, the high SFE of pure Al can be overcome to form hcp in dilute Al-Ag when the Ag preferentially "wets" an Al intrinsic stacking-fault (isf) interface,[20] and the lowest-energy structure (with *negative* SFE) is a two-layer isf-(ii) depicted in Fig. 2. This solute wetting of the SF is the local pathway for favorable formation of hcp ribbons and is consistent with the Suzuki effect.[23,24] Importantly, the local chemical structures formed around SF ribbons are shown here to determine the γ_{111} interphase boundary energy, which partly determines the equilibrium aspect ratio A_{eq}.

Recently, we obtained analytic results for the free energy of hexagonal precipitates, and we revisited the equilibrium aspect ratio of γ precipitates from a Wulff construction in a fcc solid solution.[26] Surprisingly, however, the same result that we obtained for the hexagonal plate would have equally applied to an ellipsoidal,[13,14] circular (or pillbox), or any other cross-sectional plate shape, all of which have a minimal surface free energy with *equilibrium* aspect ratio,[6]

$$A_{eq} = \frac{\gamma_{211}}{\gamma_{111}}. \tag{1}$$

Here γ_{111} is the coherent (0001)‖(111) interface energy, and γ_{211} is the incoherent $(\bar{1}100)$‖(211) interface energy, relative to fcc Al and hcp AlAg. Equation (1) arises from the surface

free energy of a hexagonal precipitate, which *increases* as $\sqrt{3}L^2\gamma_{111}+2\sqrt{3}LW\gamma_{211}$ for a given precipitate caliper length L and thickness W at a fixed critical volume.[26] Obviously, many other geometries similar to this or cylindrical pillboxes would give a similar ratio of surface terms, hence, the broad generality of the expression. The interphase energies also determine the critical nuclei dimensions of $L^* \equiv 4\gamma_{211}/\Delta G_V$ and $W^* \equiv 4\gamma_{111}/\Delta G_V$, where ΔG_V is the drop in free energy per volume upon precipitation at fixed critical volume.[26] It can be shown (also for arbitrary geometry) that the nucleation energy barrier ΔG^* is

$$\Delta G^* = \frac{16\sqrt{3}}{\Delta G_V^2}\gamma_{111}\gamma_{211}^2 \tag{2}$$

for the fixed critical volume

$$V^* = \frac{\sqrt{3}}{2}W^{*3}A_{eq}^2. \tag{3}$$

Then, of the available sites for nucleation n_A, a number

$$n^* = n_A e^{-\Delta G^*/k_B T} \tag{4}$$

is expected to become viable, where the nucleation energy barrier ΔG^* from Eq. (2) determines the nucleation rate. By rescaling in critical parameters,[26] $\tilde{L} \equiv L/L^*$ and $\tilde{W} \equiv W/W^*$, Eq. (2) gives the general shape dependence of free energy of $\Delta G^*(\tilde{L}^2+2\tilde{L}\tilde{W}-2\tilde{L}^2\tilde{W})$.

B. Nonequilibrium aspect ratio model

For the case of time-varying shapes,[7] a precipitate is able to lengthen constantly, as $\tilde{L}=1+\tilde{t}$ in dimensionless time $\tilde{t}$, so long as there are steady supplies of thin nucleating edges as shown in Fig. 3 (top structure).[26] We also showed how various growth patterns could supply the new edges.[26] However, subsequent thickening of γ plates is thought to occur only by a ledge-migration mechanism,[15] which we showed is given by $\tilde{W}=2\sqrt{1+\xi\tilde{t}}-1$. For various limits of ξ, this could give either very slow linear growth or a more rapid but plateauing $\tilde{t}^{1/2}$ growth.

The actual value of ξ is a product of four parameters and A_{eq} in Eq. (1), i.e., $\xi \equiv A_{eq}fgk\Omega$. Here $f(T)=e^{-\Delta G_h^*/k_B T}$ is a thermal rate for new ledge nucleation, g is a geometric factor between 0.5–2.3, depending on the nonequilibrium growth pattern, and $k(\Omega)$ is a factor for cylindrical solute depletion.[34,35] Finally, the *dimensionless* supersaturation Ω is[6]

$$\Omega \equiv \frac{X_0 - X_e}{X_\gamma - X_e}, \tag{5}$$

where the compositions are X_e (equilibrium depletion zone), X_γ (the precipitate), and X_0 (bulk matrix).[36] The thermal rate $f(T)$ also requires a *secondary* nucleation energy barrier,[26]

$$\Delta G_h^* = \frac{2\sqrt{3}h\gamma_{211}^2}{\Delta G_V}, \tag{6}$$

to ledges of height h. From these five basic parameters A_{eq}, $f(T)$, g, $k(\Omega)$, and Ω, any nonequilibrium growth pattern can be described almost entirely by a model combination of DFT- and analytically calculated estimates.

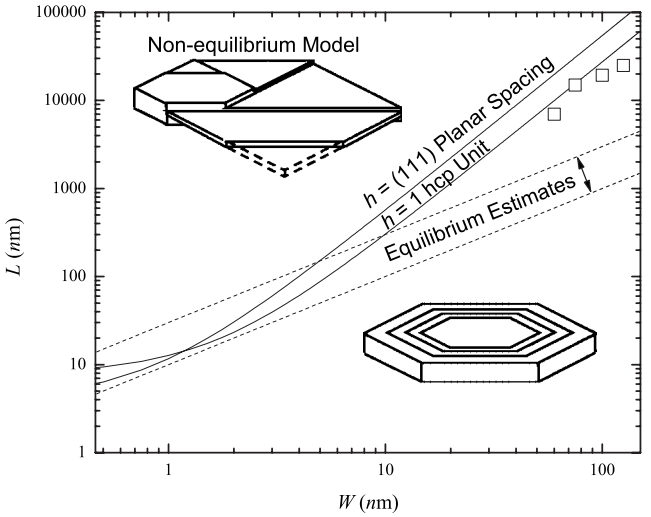

FIG. 3. Calculated length L versus thickness W of γ plates compared to experiment (Ref. 5) for Al-Ag (squares). Dashed lines are for A_{eq} from Eq. (1) with DFT-estimated interface energies. Solid lines are from Eq. (8) with $f=1$, $g=1$, $k=10$, and $\Omega=0.02$. Qualitative sketches of possible growth patterns are shown for nonequilibrium (top) and equilibrium (bottom) plates.

Using a mathematical Perrin sequence[37] to describe offshoot edges, in combination with an accepted ledge-migration model,[15] we estimated[26] the nonequilibrium aspect ratio A_{neq} for the nonequilibrium γ plates in dilute s.s. as

$$A_{neq}(t) \simeq \frac{A_{eq}+(\Omega/gkh^2)Dt}{2\sqrt{1+(f\Omega^2/h^2)Dt}-1} = \begin{cases} A_{eq}, & t \sim 0 \\ \dfrac{\sqrt{Dt/f}}{2gkh}, & t \to \infty. \end{cases} \tag{7}$$

Equation (7) depends on time t and the diffusion constant D, as well as the critical ledge nuclei height, which we can take here as just $h=W^*$, calculated from first principles. The dependence on interface energies, as in Eq. (1), is somewhat suppressed in Eq. (7) and only affects the initial shape and becomes rapidly negligible. This can be seen directly, and without the need to calculate the diffusion coefficient D (which is very expensive in DFT), by eliminating time in favor of relating spacial precipitate dimensions explicitly as

$$L(W) = A_{eq}h + \frac{W+3h}{4fgk\Omega}\left(\frac{W-h}{h}\right). \tag{8}$$

Here the initial nucleus clearly has an equilibrium shape, and as we mentioned time is linearly related to L, so we can use increasing L in Eq. (8) as a measure of time.

The growth described by this model is shown in Fig. 3 and is compared to experimental data for Al-Ag and against the (dashed line) strictly equilibrium estimates from DFT (given below). Clearly, once the precipitate dimensions exceed about 100×10 nm^2, i.e., an aspect ratio of 10, the nonequilibrium growth mechanisms rapidly outpace the equilibrium expectations, as is seen in the experimental data and in their rate of L increase versus W. Since it takes minutes for

precipitates to develop and only seconds to exceed equilibrium aspect ratios, true equilibrium shapes are only rarely observed.[7]

Both the equilibrium and nonequilibrium models require knowledge of interface energies γ_{111} and γ_{211} and the alloy phase compositions, which appear through Ω and through ΔG_h^*.

C. Temperature rescaling of parameters

The thermodynamic driving force for nucleation at finite temperature generally scales in proportion to the *critical undercooling* below the melting (solvus) temperatures T_m (T_e). We have studied several energies that scale near critical points, namely, ΔG_V, γ_{111}, γ_{211}, and the derived barriers ΔG^* and ΔG_h^* from Eqs. (2) and (6). The barriers determine the nucleation and growth rates, which control the kinetics. The rescalings that we chose are

$$\Delta G_V \to \left(\frac{T_e - T}{T_e}\right)\Delta G_V(0\ \text{K}),$$

$$\gamma_{211} \to \left(\frac{T'_m - T}{T'_m}\right)\gamma_{211}(0\ \text{K}),$$

$$\Delta G_h^* \to \left(\frac{T'_m - T}{T'_m}\right)^2\left(\frac{T_e}{T_e - T}\right)\Delta G_h^*(0\ \text{K}). \tag{9}$$

The last expression follows from Eq. (6). Also a temperature parameter $T'_m \geq T_m$ has been introduced, which we shall discuss shortly. Note that we only specify a temperature dependence for the *ledge* barrier ΔG_h^*, not the *primary* barrier ΔG^*. Its dependence on h, not on γ_{111}, is a consequence of the critical size falling below the atomic spacing.

The limits in Eqs. (9) are justified phenomenologically: (1) the rescaled ΔG_h^* vanishes at T_e, as is standard in alloy thermodynamics[6] and is often used in nucleation modeling;[38] (2) the rescaled γ_{211} vanishes at the melting temperature T'_m, assuming that a liquid layer forms preferentially at an incoherent interface. This second rescaling is approximate but should be included to be qualitatively correct.

It could perhaps be argued that at melting γ_{211} becomes $2\gamma_{SL}$, i.e., the solid-liquid interface energy, instead of zero. However, there is an opposing entropy of the liquidlike layer that diverges[39] at T_m. It is not clear how a grain-boundary energy (GBE) will behave with increasing temperature. There are various numerical simulations that illuminate this issue. First, in a Lennard-Jones molecular-dynamics study,[40] it was shown that GBE decreases *linearly* with temperature, as proposed here, and that it intersects zero at some temperature $T'_m \geq T_m$. If the energy approaches $2\gamma_{SL}$ at melting, then $T'_m = (1 - 2\gamma_{SL}/\gamma_{211})^{-1}T_m$. For coherent boundaries, such as a SF, a rescaling, such as in Eqs. (9), also holds. For example, an embedded-atom calculation at 0 and 300 K showed that Ag, Cu, and Ni have reduced SFE,[41] scaling (within 3–7 %) to the undercooling proposed here for $T'_m = T_m$. The effective melting point is also highly sensitive to pressure constraints in these types of model calculations.[42] Lastly, although grain-boundary energy is known to vary with temperature, very few experiments have examined this directly.[43] Among the limited data available, there does appear a similar trend: grain-boundary energy tends to decrease with increasing temperature, more so for high-angle misorientation and less so for low-energy cusps of orientation.

For actual numbers based on experiment,[5,30] at 4.2 at. % Ag in Al-Ag T_e is 723 K, and T_m is near 840 K for γ precipitates. This T_m sets the lower limit on T'_m in Eqs. (9). A high estimate, if not an upper bound, comes from the Lennard-Jones result[40] that suggests a value of $T'_m \simeq 2.4T_m$ ($\sim$2000 K). We will use this range of values $T'_m = 840-2000$ K and compare various limits in the following. Finally, using Eqs. (9), there is a maximal thermal rate $f(T)$ that occurs near a temperature,[26]

$$T_{opt} = \frac{T_e T'_m}{2T'_m - T_e}. \tag{10}$$

From the Al-Ag phase diagram[30] at 4.2 at. % Ag, this gives $T_{opt} = 443-633$ K, which is remarkably the range where the observed precipitation occurs.[5] At the upper end of this estimate, the energy barrier for nucleation is *halved*, which facilitates precipitation. We will discuss the temperature dependence of these energy barriers again in Sec. VI when we discuss the calculated precipitate properties.

III. ELECTRONIC-STRUCTURE CALCULATIONS

In order to study structural formation energies associated with γ precipitates, we approximate plate/matrix interfaces as SF structures. To obtain reliable energetics, we utilize the Vienna *ab initio* simulation package (VASP) (Refs. 44–47) that uses a plane-wave basis and ultrasoft pseudopotentials[48] with energy cutoffs of 275 eV, as supplied by Kresse and Hafner.[49] We used local-density approximation to the exchange-correlation functional from Ceperley and Alder,[50] as parametrized by Perdew and Zunger.[51] The VASP code calculates forces and permits structural relaxation of coordinates and cell shape. Formation energies are converged to $<$2 meV/cell with full ionic relaxation of forces to $<$30 meV/Å.

A. Computational details

For various SF structures, we used supercells based upon ordinary hexagonal cells with orthogonal c-axis orientation. For Brillouin-zone integrations, a Monkhorst-Pack[52] special k-point method is used. We converge k meshes for hexagonal cells composed on fcc (111) planes stacked along $\langle 111 \rangle$ directions, with up to $24 \times 24 \times 24$ k points in the full Brillouin zone used for primitive fcc cells. The k meshes for larger supercells are determined by condition of equal densities of points, with up to $24 \times 24 \times 8$ k points for three fcc planes along $\langle 111 \rangle$ (3 atoms/cell) and with $24 \times 24 \times 3$ k points to achieve similarly dense coverage in the longest supercells (8–15 atoms/cell). Issues of k-mesh convergence are detailed elsewhere.[20]

We find from VASP that Al and Ag have cubic lattice constants a_{fcc} of 3.98 Å and 4.02 Å, respectively. The similar *observed* lattice spacings of fcc Al (4.05 Å) and Ag

(4.09 Å) and theoretical values preclude elastic strain effects,[29] so relaxation of cell volume is generally unimportant, at least for qualitative behavior. Also there is essentially no c-axis distortion for hcp Al, so c/a is ideal, i.e., $\sqrt{8/3} \simeq 1.633$. For SF calculations, local relaxations of planes near the planar defect are important, especially with Ag segregated to the fault; whereas, for large ⟨111⟩-layered supercells with a SF, the cell volume relaxation with the planar defect is negligible, as expected. For the inhomogeneous Al-Ag alloys that we investigate, we use a_{fcc}=3.98 Å, giving 6.86 Å^2 for the common per atom (111) planar area A_{111}. As in previous studies,[53] five planes are enough to converge SFE for pure Al to ±10 mJ/m^2; but in the Al-Ag alloy, Ag impurity planes may be situated directly between the SF and its periodic image, giving poor separation between impurities, defects, and their periodic images. For this reason, we use 11 atomic planes for isf, as a fcc ⟨111⟩ planar defect shown in Fig. 2. Cell size used here ensures reliable energies as impurity planes vary in distance from the SF (see Ref. 20 for details).

B. SFE in inhomogeneous solid solutions

Stacking faults, such as the important isf initiated during shear, are local hcp deviations from fcc (111) stacking,[20] as shown in Fig. 2. The planar SFE (in units of mJ/m^2) is thus the energy to shear fcc into local hcp. We calculated the SFE versus Ag content for inhomogeneous distributions of Ag, such as layered Ag (111)-planes adjacent to SF, and compared it to a homogeneous Al-Ag s.s. from a cluster expansion.[54] As found in Ref. 20, the structures at 0 K with lowest SFE have alternating Al/Ag (111) planes within a tungsten-carbide (WC) structure embedded in Al matrix, as shown in Figs. 2 and 4(a). Here we repeat these calculations with the modification of finite-temperature point entropy added to the s.s. curves in Fig. 4(b). In contrast to our previous 0 K results, we find that at experimental temperatures, the s.s. competes with ordered compounds in thermal equilibrium; however the inherent asymmetry of the hcp and fcc s.s. curves leaves hcp slightly higher for most Al-rich compositions. Equilibrium is thus established between alternating Al/Ag-hcp and α-fcc Al.

C. Precipitation parameters from first principles

For a binary alloy near 0 K, entropic effects are negligible. Therefore, $\Delta G(0\ \mathrm{K})$ is given by the change in total internal energy of the alloy ΔE. The ΔE is proportional to the number of atoms in the alloy but is equivalently defined in terms of the *formation energy per atom* ΔE_f relative to phase-segregated species. Taking our prototype system of Al-Ag, ΔE_f is defined with respect to fcc endpoint elements as

$$\Delta E_f = \frac{E^{\mathrm{Al\text{-}Ag}}}{N} - \left(\frac{N-m}{N} E^{\mathrm{Al}}_{fcc} + \frac{m}{N} E^{\mathrm{Ag}}_{fcc} \right), \qquad (11)$$

where E is the total alloy internal energy, N is the total number of atoms, m is the number of Ag impurities, and E^{α}_{fcc} is the fcc energy per constituent atom. For Al-Ag, specifically, with Ag segregating to a SF in parallel layers, we note that N and m are equivalently the number of layers and Ag layers, respectively, in the unit cell along ⟨111⟩ (see Fig. 2). Free energies of formation ΔG_f are defined analogously to Eq. (11), substituting reference energy G^{Al}_{fcc} (G^{Ag}_{fcc}) for E^{Al}_{fcc} (E^{Ag}_{fcc}). Formation energies for hcp and fcc s.s. and ground-state (GS) structures at T=0 are shown in Fig. 4(a) and listed in Table I. Also shown are the SFEs, which are neither hcp nor fcc, but rather they are ribbons of hcp embedded in fcc matrix.

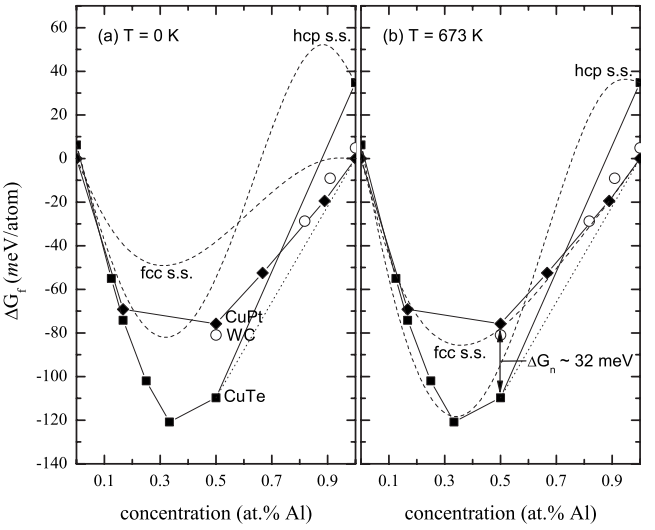

FIG. 4. VASP ΔG_f (meV/atom) of fcc and hcp relative to fcc Al and Ag, with ground states of fcc-based (diamond) and hcp-based (square) systems and fcc and hcp solid solutions (s.s.), dashed lines from Ref. 54. Along with hcp tungsten-carbide (WC) structure, we show the isf (open circles) of varying composition with local Ag arrangement similar to WC. The fcc and hcp ground states intersect at $X_{\mathrm{Ag}} \sim 0.22$, the observed maximum solubility of Ag in Al (Ref. 30). At X_{Ag}=0.50, hcp AlAg is favorable over all fcc structures (dotted Maxwell tie lines).

From Fig. 2, the $\Delta E_f^{isf-(ii)}$ per atom for a cell of $N_{isf-(ii)}$ atomic planes is the formation energy ΔE_f^{WC} per atom of *four* hcp AlAg planes plus *two* γ_{111} interfaces, which gives

$$\gamma_{111} = \frac{N_{isf-(ii)} \Delta E_f^{isf-(ii)} - 4\Delta E_f^{WC}}{2A_{111}}. \qquad (12)$$

Similarly, the γ_{211} interfaces hcp AlAg with fcc Al, as illustrated in Fig. 5. This is simulated on a N_{211}=24 atom cell

TABLE I. VASP formation energy ΔE_f (in meV/atom) relative to fcc and planar defect energy γ_{isf} (in mJ/m^2) to form isf between (111)-planes in fcc Al. The isf-(i) and isf-(ii) have one and two Ag layers, respectively, in alternating Al/Ag (111) planes. These four structures are indicated by open circles in Fig. 4. Results are calculated for 6-atom hcp and 11-atom isf.

at. % Al	Structure	ΔE_f	γ_{isf}
1.00	isf	+5.3	137
0.91	isf-(i)	−8.1	137
0.82	isf-(ii)	−27.2	−50
0.50	WC	−78.0	−22

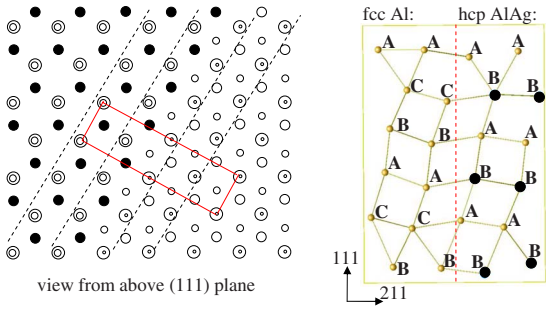

FIG. 5. (Color online) The (211) interface between hcp AlAg and fcc Al; light (dark) circles are Al (Ag). (Left) viewed along [111] on (111), where circle size indicates stacking out of the plane; (right) viewed as a cross section projected onto (110), where the interface approximates edges parallel to [110] of γ precipitates. A distorted fcc "*ABC*" (hcp "*AB*") stacking is indicated.

with 12 fcc Al and 12 hcp AlAg, which gives

$$\gamma_{211} = \frac{N_{211}\Delta E_f^{211} - 12\Delta E_f^{WC}}{2A_{211}}. \quad (13)$$

IV. INTERFACE ENERGIES AND PRECIPITATE SHAPE

The (111) broad face of a γ precipitate, which is the (0001) basal plane of hcp precipitate, is expected to have low γ_{111}, encouraging lateral growth and long thin plates. Often in the past (see, e.g., Ref. 28), it was assumed that γ_{111} for dilute Al-Ag was similar to $\gamma_{SF}^{Al} \sim 130$ mJ/m^2, which cannot be the case because high SFE inhibits nucleation. As discussed earlier, Ag wetting the SF greatly reduces the SFE, indicating that Ag wetting is important for low γ_{111}. If the γ_{111} is vanishing or negative, the equilibrium plate shape has infinite-aspect ratio. However, observed precipitates thicken even as aspect ratio increases,[5] suggesting a small but positive value for γ_{111} that encourages lateral growth.

Here we model the precipitate-matrix interface as alternating AlAg hcp, as in Fig. 2. Before the precipitates were measured to have X_γ=0.40–0.50, Howe[55] proposed a structure of alternating pure Ag and Al_2Ag to explain observed 000*l*, with *l* being *odd* long-range order reflections in [111]$\|$[0001] x-ray diffraction patterns. However, $X_\gamma \sim 0.46 \pm 0.04$ is now observed,[5] which is in agreement with theory, due to recalibration of reference. Thus, the hcp AlAg structure is consistent with both recently observed X_γ and older diffraction data,[55] as there is alternating structure of Ag on every other plane. Using VASP results in Eq. (12) for $\Delta E_f^{isf-(ii)}$ and ΔE_f^{WC} (Table I), we obtain $\gamma_{111} = 15 \pm 10$ mJ/m^2. We address the small magnitude of this interface energy later on, where it is found to place strict limits on the critical ledge height *h* in Eqs. (6), (7), and (9).

The calculated (211) interface energy using VASP is $\gamma_{211} = 325 \pm 10$ mJ/m^2. Early estimates[28,33] for the hcp-fcc disordered interface energy find values, ranging between 350–500 mJ/m^2 or comparable to the measured[19] Al GBE of 324 mJ/m^2.

Knowing γ_{211} and γ_{111} gives an estimate of $A_{eq} \sim 20$ from Eq. (1). Early overestimates of γ_{111} as the pure Al SFE (Refs. 28 and 31) of 120–180 mJ/m^2 led to predictions[31,32] of an aspect ratio of $A_{eq} \sim 3$, smaller than observed by at least an order of magnitude.[5] Our aspect ratio is larger but still 10 $\times$less than experiment, which led to our proposal[26] of a nonequilibrium model for A_{neq} in Eqs. (7) and (8) and in Fig. 3. A large A_{eq} enhances A_{neq}, initially, but not by much and only for a short time. Clearly, γ plates in Al-Ag must break symmetry to develop rapidly, requiring a rapid nucleation of edges and ledges. Our parameters are listed in Table II.

TABLE II. Nucleation parameters for γ precipitates in Al-Ag from theoretical estimates, experimentally assessed, and present model with numerical values obtained using VASP.

Parameters	Estimate/analytic	Experiment	Present work
X_γ (at. % Ag)	0.67[a,b]	0.46 $\pm$ 0.04 [c]	0.50
ΔG_V (MJ/m^3)	337[b], 250		330 $\pm$ 20
γ_{111} (mJ/m^2)	120[d]		15 $\pm$ 10
γ_{211} (mJ/m^2)	500[b], 350[d]	324[e]	325 $\pm$ 10
L^* (nm)	3.40[b]		4.0 $\pm$ 0.5
W^* (nm)	0.47[b]	0.46[d]	0.2 $\pm$ 0.1
A_{eq}	2.7[a], 7.2[b]		20 $\pm$ 10
A_{neq}		40–330[c]	>300
ΔG^* (eV)			2.5 $\pm$ 1.5
ΔG_h^* (eV)	7[b], 12		1.6 $\pm$ 0.2
$\Delta G_h^*[T_{opt}]$ (eV)			0.8 $\pm$ 0.1
T_{opt} (°C)		400[c]	170–360

[a]Model for Ostwald ripening of disks, X_γ=0.67 (Ref. 31).
[b]Analysis of growth ledge nucleation, X_γ=0.67 (Ref. 33), 0.50 corrected.
[c]TEM experiment (Ref. 5).
[d]Experiment via analysis of growth ledges and interface energy (Ref. 28).
[e]Measured Al grain-boundary interface energy (Ref. 19).

V. FREE-ENERGY ESTIMATION

The usefulness of free energy is demonstrated by the dotted *Maxwell construction* line in Fig. 4. Tangents to free-energy curves describe the relative phase stability for each structure. The free-energy curves for GS Al-Ag phases share an approximate common tangent, as indicated by the dotted line in Fig. 4. The lowest-energy hcp structure is Ag_2Al. However, from a common-tangent construction, equilibrium is established with hcp AlAg.

The equilibrium phases of hcp and fcc Al-Ag are key for predicting thermodynamic and kinetic properties of γ-phase AlAg precipitates. The zero-temperature energy diagram in Fig. 4(a) predicts a solute fraction X_γ of 0.50 for the AlAg γ phase. Until recently,[54] an assumption that plates were ordered Ag_2Al (X_γ=0.67) was always used in data analysis,[31–33] as suggested by the assessed equilibrium phase diagram.[30] However, recent observations by Moore and Howe[5] find X_γ=0.46 $\pm$ 0.04, determined by edge-on energy-dispersive x-ray spectroscopy and averaged over 17 plates at T=673 K. The value $X_\gamma \sim 0.46$ agrees more with the *ab ini-*

tio result $X_\gamma=0.50$ in Table II and the calculated phase diagram.[54]

Since entropy is negligible for ordered GS compounds compared to s.s., the energies of ordered GS curves can be treated as nearly identical to $T=0$ results. The resulting curves obtained by adding mixing energies to s.s. are shown for $T=673$ K in Fig. 4(b). Finite-temperature s.s. curves are lower with increasing temperature. The s.s. curves cross the ordered GS curves at 673 K. Also the GS and fcc s.s. are essentially degenerate below $X_{Ag}=0.50$, sharing an approximately linear shape. Dilute Al-Ag s.s. quenched from high temperature *initially* lies along that linear portion of the fcc s.s. curve in Fig. 4. So, by common-tangent construction, dilute fcc is in approximate chemical equilibrium with fcc structures down to 50% Ag, i.e., as a mix of dilute fcc s.s. and hcp precipitates. The fcc s.s. and hcp GS energy difference gives the *driving force* for precipitation ΔG_n [see Fig. 4(b)].

Exploiting the linearity of fcc energies, the tangent to fcc s.s. for dilute Al-Ag connected to s.s. fcc near $X_{Ag}=0.50$ gives $\Delta G_n \approx 32$ meV/atom. Alternately, we approximate ΔG_n by the $T=0$ hcp-fcc GS structural energy difference of 34 meV/atom. Averaging these two estimates, we get $\Delta G_n \simeq 33 \pm 2$ meV/atom. Finally, using the atomic volume $V_a = a_{fcc}^3/4$ and $a_{fcc} \simeq 4$ Å, the driving force *per unit volume* ΔG_V is $\Delta G_n / V_a \simeq (330 \pm 20) \times 10^6$ J/m^3.

For comparison, the driving force ΔG_V was previously estimated, for dilute s.s.,[31–33] as

$$\Delta G_V \approx \frac{X_\gamma - X_e}{1 - X_e} \frac{k_B T}{V_a} \ln\left(\frac{X_0}{X_e}\right), \tag{14}$$

where X_0 and $X_e < X_0$ are the overall alloy content and fcc equilibrium solute fraction, respectively. Reference 33 applies Eq. (14) to Al-Ag with $X_0=0.052$ and $X_e=0.021$ at $T=679$ K, giving a driving force of 340×10^6 J/m^3. This result depends explicitly on precipitates being Ag_2Al and thus should not be compared with present *ab initio* result. Altering the analysis to use the correct $X_\gamma=0.50$ in Eq. (14) for AlAg precipitates yields 250×10^6 J/m^3—understandably less than our result since Eq. (14) ignores enthalpy of mixing.

VI. *AB INITIO* ESTIMATED PRECIPITATE PROPERTIES

Using our free-energy model,[26] we find that precipitate nuclei less than $0.5W^*$ thick fail to grow. For precipitate nuclei near W^* thickness, there is a saddle point in the free-energy surface, a minimum-energy barrier ΔG^*. Using our *ab initio* calculated value for driving force ΔG_V of $(330 \pm 20) \times 10^6$ J/m^3 and γ_{111} of 15 mJ/m^3, we find that the critical nuclei thickness W^* is 1–3 Å (see Table II). This value for W^* is small compared to the physically allowable plate thickness, e.g., compared to the close-packed (111)-planar spacing in Al-Ag $a_{fcc}/\sqrt{3}=2.30$ Å or the hcp c-axis repeat unit $2a_{fcc}/\sqrt{3}=4.60$ Å. For h, these physical lower bounds must replace the actual calculated value for critical nuclei thickness to obtain sensible results. Of course, similarity of W^* to the (111) planar spacing has very little meaning in the continuum model, but it does suggest that even a single atomic (111) plane is sufficient for nucleation.

In addition to critical thickness W^*, we find that the critical volume V^* from Eq. (3) is 10^3–10^4 Å^3, where we have used the calculated values for $W^* \sim 1$–3 Å. The critical number of atoms n^* per nuclei is obtained from Eq. (3) and the volume per atom $a_{fcc}^3/4$, which give

$$n^* = \frac{V^*}{a_{fcc}^3/4} = 2\sqrt{3} A_{eq}^2 \left(\frac{W^*}{a_{fcc}}\right)^3. \tag{15}$$

This places an upper bound on the density of nucleation sites, using our calculated parameters: if nucleation begins on more than one site out of $n^* \sim 10$–10^3 sites, overlapping solute depletion inhibits precipitation. This simply means that if two nuclei grow within a volume V^*, corresponding to n^* atoms available for local precipitation, the two nuclei will intersect, in which case they will become *impinged*, as discussed, e.g., in Ref. 33. Importantly, the omission of impingement is why the nonequilibrium model might overestimate A_{neq}.

Finally, the nucleation barrier ΔG^* in Eq. (2) is 2.5 ± 1.5 eV. At $T=673$ K, we have $k_BT=0.058$ eV and $\Delta G^* \sim 20$–$70 k_BT$ (see Table II). For a given number of nucleation sites n_A, the number n^* of critical nuclei is given by Eq. (4). The fraction of available nucleation sites producing viable nuclei is less than $e^{-20} \sim 10^{-9}$. However, since the *ledge* nucleation barrier $\Delta G_h^* \sim 20$–$30 k_BT$ is necessarily half as large (half the broad facial area), the fraction of viable *ledge* nucleation sites increases; using the temperature rescaling of Eqs. (9) and (10) in Table II, we get two ranges of estimates: first near 170 °C, $\Delta G_h^* \simeq 60$–$80 k_B T_{opt}$ and second near 360 °C, $\Delta G_h^* \simeq 10$–$20 k_B T_{opt}$. Clearly, the latter condition is dramatically more favorable and suggests the more rapid reduction of γ_{211} with increasing temperature within our model. Under the most optimal annealing conditions ($T_{opt}=360$ °C and an entropy-driven vanishing of γ_{211} at melting), the fraction of viable sites would thus begin to approach an appreciable fraction $e^{-10} \sim 10^{-5}$, which is an upper limit. The effective temperature in the exponential in this case is $T_e T_m / 4(T_m - T_e) \sim 1000$ °C (or 0.1 eV), accounting for the reduction by a factor of 2 of the energy barrier. These are rough estimates but clearly provide a better argument than before that a classical nucleation picture can be supported. Lastly, for *heterogeneous* nucleation assisted by defects, the energy barrier ΔG_h^* may be instantly overcome by the nucleation on a SF ribbon of high energy ~130 mJ/m^2 on small areas of 10–100 planar atoms, quenched in from solid solution.

VII. ADSORBATE ISLAND GROWTH

Before concluding, we relate our derived model of γ-precipitate growth along fcc ⟨111⟩ to the growth of islands composed of surface adsorbates or surface-segregated atoms forming islands on fcc(111) surfaces. Similar to the growth patterns of γ plates,[7] the shapes of Ag islands on Al(111) bear a striking resemblance to those clipped triangles considered here (compare Fig. 3 to figures in Refs. 8–10). Nontriangular oblong shapes are grown on other substrates, e.g.,

Si(111).[11] For all islands on surfaces, the free-energy arguments are generically similar to those presented here for γ plates; considering a plate nucleated on a surface, $\gamma_{111} \rightarrow (\gamma_a - \gamma_s + \gamma^*)/2$, where γ_a, γ_s, and γ^* are the adsorbate, substrate, and interfacial surface energies, respectively. We did not yet perform a detailed calculation for any specific islands. However, as an estimate for Al and Ag, the calculated surface free-energy difference $\gamma_a - \gamma_s$ must be small and negative (estimated as -30 mJ/m^2 in Ref. 56), and the value of γ^* is likely very small and positive (estimated here as 15 mJ/m^2). The near cancellation of $\gamma_a - \gamma_s$ and γ^* will lead to a competition between smooth layer-by-layer growth versus rough 3-*d* growth, which is what is seen experimentally. Here, the comparison to bulk systems is limited to the similarity of surface free energies at play; however, as strain/relaxation effects are likely to be of much greater importance for island coarsening, these should be included for more general conclusions.

VIII. SUMMARY AND CONCLUSION

We have proposed a model for many aspects of hcp precipitates in fcc alloys, which is based on classical nucleation theory in combination with symmetry breaking. Using first-principles DFT, we created supercells to obtain approximate coherent and incoherent interphase energies, and we determined supersaturation of the solute in the precipitate from finite-temperature free energies. Using these results, we applied the analytic model to an experimentally well-studied prototype of fcc Al-Ag solid solution, where high-aspect ratios of greater than 300 are observed within hundreds of seconds.[5] Many previous models have addressed this, but none have accurately fit the rapid aspect ratio development nor have any predicted an equilibrium aspect ratio larger than 10. Here, we have accomplished both and relate the two cases based on our proposed nonequilibrium growth, with input determined directly from DFT calculations. We find aspect ratios >300 in agreement with the most recent *in situ* experiment,[5] as well as a host of other precipitate properties previously inaccessible to experiment. The approach is general to other precipitate morphologies, as well as related to island coarsening.

ACKNOWLEDGMENTS

Funding was provided by the Office of Naval Research and Department of Energy Grants No. DEFG02-03ER46026 and No. DEFG02-91ER45439 at the Frederick Seitz Materials Research Laboratory. We acknowledge computing support by DOE and an INTEL computer grant.

*finkenst@usna.edu
†duanej@illinois.edu

[1] A. Guinier, Nature (London) **142**, 569 (1938).
[2] G. D. Preston, Nature (London) **142**, 570 (1938).
[3] A. Guinier, J. Phys. Radium **3**, 124 (1942).
[4] R. B. Nicholson and J. Nutting, Acta Metall. **9**, 332 (1961).
[5] K. T. Moore and J. M. Howe, Acta Mater. **48**, 4083 (2000).
[6] D. A. Porter, K. E. Easterling, and M. Y. Sherif, *Phase Transformations in Metals and Alloys*, 3rd ed. (Taylor and Francis Group, Boca Raton, 2009).
[7] T. J. Konno, E. Okunishi, T. Ohsuna, and K. Hiraga, J. Electron Microsc. **53**, 611 (2004).
[8] V. Fournée, J. Ledieu, T. Cai, and P. A. Thiel, Phys. Rev. B **67**, 155401 (2003).
[9] A. Courty, A.-I. Henry, N. Goubet, and M.-P. Pileni, Nature Mater. **6**, 900 (2007).
[10] P. A. Thiel, M. Shen, D.-J. Liu, and J. W. Evans, J. Phys. Chem. C **113**, 5047 (2009).
[11] Y. Li, M. Liu, D. Ma, D. Yu, X. Chen, X.-C. Ma, Q.-K. Xue, K. Xu, J.-F. Jia, and F. Liu, Phys. Rev. Lett. **103**, 076102 (2009).
[12] C. Zener, J. Appl. Phys. **20**, 950 (1949).
[13] F. S. Ham, J. Phys. Chem. Solids **6**, 335 (1958).
[14] G. Horvay and J. W. Cahn, Acta Metall. **9**, 695 (1961).
[15] G. J. Jones and R. K. Trivedi, J. Appl. Phys. **42**, 4299 (1971).
[16] G. Spanos, R. A. Masumura, R. A. Vandermeer, and M. Enomoto, Acta Metall. Mater. **42**, 4165 (1994).
[17] G. Chen, G. Spanos, R. A. Masumura, and W. T. Reynolds, Jr., Acta Mater. **53**, 895 (2005).
[18] J. Z. Liu, A. van de Walle, G. Ghosh, and M. Asta, Phys. Rev. B **72**, 144109 (2005).
[19] L. E. Murr, *Interfacial Phenomena in Metals and Alloys* (Addison-Wesley, Reading, MA, 1975).
[20] D. Finkenstadt and D. D. Johnson, Phys. Rev. B **73**, 024101 (2006).
[21] S. A. Kibey, J. B. Liu, D. D. Johnson, and H. Sehitoglu, Acta Mater. **55**, 6843 (2007).
[22] M. Jahnátek, J. Hafner, and M. Krajčí, Phys. Rev. B **79**, 224103 (2009).
[23] H. Suzuki, J. Phys. Soc. Jpn. **17**, 322 (1962).
[24] J. P. Hirth and J. Lothe, *Theory of Dislocations* (McGraw-Hill, New York, 1968).
[25] S. A. Kibey, L. L. Wang, J. B. Liu, H. T. Johnson, H. Sehitoglu, and D. D. Johnson, Phys. Rev. B **79**, 214202 (2009).
[26] D. Finkenstadt and D. D. Johnson, Mater. Sci. Eng., A **525**, 174 (2009).
[27] Reprinted with permission from Ref. 5, Fig. 6, Copyright Elsevier (2000).
[28] C. Laird and H. I. Aaronson, Acta Metall. **17**, 505 (1969).
[29] N. W. Ashcroft and N. D. Mermin, *Solid State Physics*, 1st ed. (Saunders College Publishing, Fort Worth, 1976).
[30] A. McAlister, Bull. Alloy Phase Diagrams **8**, 526 (1987).
[31] M. Ferrante and R. D. Doherty, Acta Metall. **27**, 1603 (1979).
[32] K. E. Rajab and R. D. Doherty, Acta Metall. **37**, 2709 (1989).
[33] R. D. Doherty and K. E. Rajab, Acta Metall. **37**, 2723 (1989).
[34] M. Enomoto and H. I. Aaronson, J. Appl. Phys. **51**, 818 (1980).
[35] For a cylinder $k(\Omega) = \sqrt{(3/2)^2 + 3/\Omega} - 3/2$ ($\simeq 10$ for $\Omega \sim 0.02$).
[36] Ω is from phase diagram (Ref. 30) or solute concentration; in Ref. 5, solute depletion is $X_0 - X_e \sim 0.01$ and plate composition is $X_\gamma \sim 0.5$, which for dilute samples gives $\Omega \sim 0.02$.
[37] R. Perrin, L'Intermed. Math. **6**, 76 (1899).

[38] J. R. Jeffries, K. J. M. Blobaum, M. A. Wall, and A. J. Schwartz, Phys. Rev. B **80**, 094107 (2009).
[39] R. Kikuchi and J. W. Cahn, Phys. Rev. B **21**, 1893 (1980).
[40] J. Q. Broughton and G. H. Gilmer, Phys. Rev. Lett. **56**, 2692 (1986).
[41] R. Meyer and L. J. Lewis, Phys. Rev. B **66**, 052106 (2002).
[42] W. Fan and X.-G. Gong, Phys. Rev. B **72**, 064121 (2005).
[43] H. Miura, M. Kato, and T. Mori, J. Mater. Sci. Lett. **13**, 46 (1994).
[44] G. Kresse and J. Hafner, Phys. Rev. B **47**, 558 (1993).
[45] G. Kresse and J. Furthmuller, Comput. Mater. Sci. **6**, 15 (1996).
[46] G. Kresse and J. Furthmuller, Phys. Rev. B **54**, 11169 (1996).
[47] G. Kresse and D. Joubert, Phys. Rev. B **59**, 1758 (1999).
[48] D. Vanderbilt, Phys. Rev. B **41**, 7892 (1990).
[49] G. Kresse and J. Hafner, J. Phys.: Condens. Matter **6**, 8245 (1994).
[50] D. M. Ceperley and B. J. Alder, Phys. Rev. Lett. **45**, 566 (1980).
[51] J. P. Perdew and A. Zunger, Phys. Rev. B **23**, 5048 (1981).
[52] H. J. Monkhorst and J. D. Pack, Phys. Rev. B **13**, 5188 (1976).
[53] Y. Mishin, D. Farkas, M. J. Mehl, and D. A. Papaconstantopoulos, Phys. Rev. B **59**, 3393 (1999).
[54] N. A. Zarkevich and D. D. Johnson, Phys. Rev. B **67**, 064104 (2003).
[55] J. M. Howe, U. Dahmen, and R. Gronsky, Philos. Mag. A **56**, 31 (1987).
[56] L. Vitos, A. V. Ruban, H. L. Skriver, and J. Kollar, Surf. Sci. **411**, 186 (1998).